Fitting the Five-Term Semi-Empirical Mass Formula to the AME2020 Atomic Mass Evaluation: Best-Fit Coefficients, Case Studies, and the Shell-Structure Residual Signature

July 21, 2026

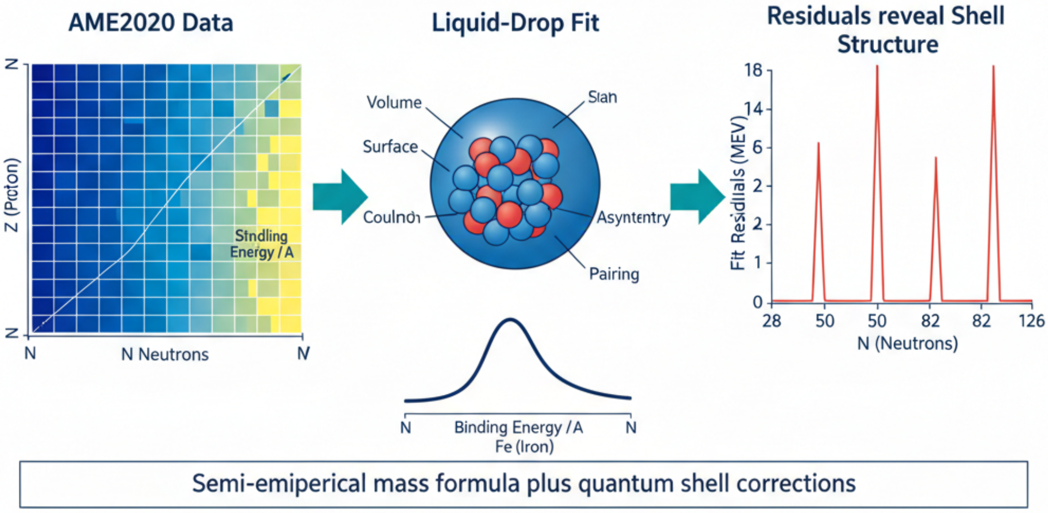

Figure 1: Graphical abstract. Workflow of this study. Binding energies for all $A \geq 16$ nuclei are extracted from the AME2020 atomic mass evaluation (left); the five-term liquid-drop (Bethe–Weizsäcker) mass formula is fitted to the total binding energies by unweighted least squares (centre); and the fit residuals, plotted against neutron number, reveal sharp positive spikes at the magic numbers $N = 28, 50, 82, 126$ (right)—the fingerprint of quantum shell structure that the macroscopic model cannot capture and that motivates the microscopic shell model.

Abstract

We extract the binding energy per nucleon of every nuclide with mass number $A \geq 16$ from the AME2020 atomic mass evaluation (release dated 3 March 2021; *Chinese Physics C* **45**, 030002/030003) published by the IAEA Atomic Mass Data Center, and fit the five-term semi-empirical (liquid-drop) mass formula—volume, surface, Coulomb, asymmetry, and pairing—to the total binding energies by unweighted ordinary least squares. Using the full set of 3487 nuclei (including AME extrapolated values) we obtain volume $a_v = (15.296 \pm 0.018)\,\text{MeV}$, surface $a_s = (16.357 \pm 0.056)\,\text{MeV}$, Coulomb $a_c = (0.6917 \pm 0.0012)\,\text{MeV}$, asymmetry $a_a =$

(22.30 ± 0.04) MeV, and pairing $a_p = (11.39 \pm 0.87)$ MeV, values fully consistent with accepted literature. The model reproduces total binding energies with a root-mean-square (RMS) deviation of the predicted binding energy *per nucleon* of 0.0762 MeV/nucleon across all fitted nuclei ($R^2 = 0.99995$ on total E_B). For the case studies, ^{56}Fe is slightly *over*predicted (494.80 MeV vs. measured 492.26 MeV; error -2.54 MeV, -0.52%), whereas the doubly-magic ^{208}Pb is systematically *under*predicted (1625.23 MeV vs. measured 1636.43 MeV; error $+11.20$ MeV, $+0.68\%$). Plotting the per-nucleon residuals against neutron number N exposes pronounced positive peaks at the magic neutron numbers $N = 28, 50, 82, 126$, where the model most systematically fails. The responsible physical effect is nuclear *shell structure*: the closure of a major neutron shell produces extra binding that the smooth macroscopic liquid-drop model omits by construction, and which is recovered only by the microscopic shell model or by macroscopic–microscopic shell corrections.

1 Introduction

The atomic nucleus is a strongly correlated quantum many-body system whose ground-state mass encodes the net result of the nuclear, Coulomb, and symmetry interactions among its constituent nucleons. The mass defect, or equivalently the total binding energy $E_B(Z,N) = [Z\, m_{\mathrm{H}} + N\, m_n - M(Z,N)]\,c^2$, is one of the most precisely measured quantities in all of physics and constitutes the primary experimental constraint on theories of nuclear structure [1]. Its smooth systematic variation with proton number Z and neutron number N was already recognised in the earliest days of nuclear physics, when Gamow proposed that a nucleus behaves like a charged, incompressible liquid drop held together by short-range attractive forces and destabilised by surface tension and Coulomb repulsion [2]. This intuitive picture was placed on a quantitative footing by von Weizsäcker, whose 1935 semi-empirical mass formula expressed the binding energy as a sum of bulk (volume), surface, Coulomb, and asymmetry contributions, later supplemented by a pairing term [3]. Bethe and Bacher codified the approach in their landmark review [4], and the same liquid-drop energy functional underpinned Bohr and Wheeler's theory of nuclear fission [5]; the resulting expression is universally known as the Bethe–Weizsäcker, or semi-empirical mass, formula (SEMF).

The SEMF is a *macroscopic* model: it treats the nucleus as a classical drop of nuclear matter and, with only five adjustable coefficients, reproduces the binding energies of thousands of nuclei to a precision of a few parts in a thousand. It correctly predicts the characteristic shape of the binding-energy-per-nucleon curve, which rises steeply for light nuclei, reaches a broad maximum of about 8.8 MeV/nucleon near ^{56}Fe, and declines gently towards the heaviest elements—the curve that simultaneously explains why energy is released both in the fusion of light nuclei and in the fission of heavy ones. Yet the very smoothness that makes the liquid-drop model so economical is also its principal limitation. Nucleons are fermions filling discrete quantum orbitals, and when the neutron or proton number equals one of the "magic" values $2, 8, 20, 28, 50, 82, 126$ a major shell closes, conferring anomalous stability that no smooth function of A and Z can reproduce. The independent discovery of these magic numbers and their explanation in terms of a strong spin–orbit interaction by Goeppert Mayer [6] and by Haxel, Jensen, and Suess [7] launched the microscopic nuclear shell model, later developed in depth by Bohr and Mottelson [8]. The modern reconciliation of the two pictures is the macroscopic–microscopic method, in which a liquid-drop energy is augmented by Strutinsky shell corrections [9, 10]; this scheme underlies the finite-range droplet model (FRDM) [11, 12], the Weizsäcker–Skyrme mass models [13], the microscopic Duflo–Zuker mass formula [14], and self-consistent Hartree–Fock–Bogoliubov mass tables [15].

Accurate nuclear masses remain of central importance well beyond nuclear structure itself. They set the energetics of the astrophysical rapid neutron-capture (r-)process that forges roughly half of the elements heavier than iron, and the propagation of mass uncertainties is one of the dominant systematic errors in r-process nucleosynthesis calculations [16, 17]. The definitive compilation of experimental masses is the Atomic Mass Evaluation, whose 2020 edition (AME2020) provides a self-consistent least-squares adjustment of all available mass measurements [18, 19] and is distributed together with the companion NUBASE2020 nuclear-properties evaluation [20]. Precisely because the SEMF is simple, transparent, and still remarkably accurate, it continues to serve as the reference macroscopic baseline against which shell effects are defined, as the starting point for parameter-correlation studies [21, 22], and increasingly as a physics-informed prior for machine-learning mass models [23, 24].

In this report we perform a clean, reproducible determination of the five SEMF coefficients from the AME2020 data set restricted to $A \geq 16$, quantify how well the fitted model describes the binding energy per nucleon, examine two benchmark nuclei—the abundance peak ^{56}Fe and the doubly-magic ^{208}Pb—and analyse the fit residuals as a function of neutron number. The residual analysis makes the breakdown of the macroscopic model directly visible and localises it precisely at the magic neutron numbers, providing a textbook demonstration of the transition from the liquid-drop model to the shell model.

2 Data and Methodology

2.1 Data set: the AME2020 mass table

The binding-energy data were taken from the AME2020 atomic mass evaluation, the mass table published by the IAEA Atomic Mass Data Center. Specifically, we used the machine-readable file `mass_1.mas20.txt` distributed by the AMDC; its internal header carries the release stamp **3 March 2021**, corresponding to the published evaluation of Huang, Wang, Kondev, Audi, and Naimi in *Chinese Physics C* **45** (2021) 030002 (Part I, input data and adjustment procedures) and Wang *et al. Chinese Physics C* **45** (2021) 030003 (Part II, tables and graphs) [18, 19]. AME2020 supersedes the previous AME2016/NUBASE2016 evaluation [25] and incorporates the many high-precision Penning-trap and storage-ring mass measurements reported in the interim. **The release of the mass table used in this work is therefore AME2020 (dated 3 March 2021).**

The file was parsed according to the documented fixed-width Fortran record format. For each nuclide we extracted the proton number Z, neutron number N, mass number A, and the tabulated BINDING ENERGY/A column (with its quoted uncertainty), which the AME provides directly in keV and which we converted to MeV. The binding energy per nucleon and the total binding energy are related by $E_B = A\,(E_B/A)$. Three data-handling rules were applied. First, the internal consistency $N + Z = A$ was verified for every record. Second, the data were restricted to $A \geq 16$ as required, removing the lightest 71 nuclides for which the macroscopic liquid-drop approximation is least appropriate; this leaves 3487 nuclei. Third, AME entries whose values are theoretical extrapolations rather than measurements (flagged in the file by a `#` symbol in place of the decimal point) were retained but tagged with an `is_estimated` flag, so that the fit could be performed either on the complete set or on measured values only. Of the 3487 nuclei with $A \geq 16$, 2484 carry experimentally determined masses and 1003 are AME extrapolations.

The parser was validated against rounded literature values of the binding energy per nucleon for three reference nuclei, all of which agree to within 0.001 MeV/nucleon: ^{16}O (7.9762 vs. 7.976), ^{56}Fe (8.7904 vs. 8.790), and ^{208}Pb (7.8675 vs. 7.867 MeV/nucleon).

2.2 The five-term semi-empirical mass formula

We adopt the standard five-term Bethe–Weizsäcker parameterisation of the total binding energy,

$$E_B(Z,N) \;=\; a_v A \;-\; a_s A^{2/3} \;-\; a_c \frac{Z(Z-1)}{A^{1/3}} \;-\; a_a \frac{(A-2Z)^2}{A} \;+\; \delta(Z,N), \tag{1}$$

in which the five physical contributions are, in order: the *volume* term $a_v A$, expressing the saturation of the nuclear force so that each nucleon in the bulk contributes a constant binding; the *surface* term $-a_s A^{2/3}$, a negative correction for nucleons at the surface which have fewer neighbours, scaling with the surface area $\propto A^{2/3}$; the *Coulomb* term $-a_c Z(Z-1)/A^{1/3}$, the electrostatic repulsion of a uniformly charged sphere of radius $R \propto A^{1/3}$, where the factor $Z(Z-1)$ counts distinct proton pairs and thereby removes the unphysical proton self-interaction; the *asymmetry* (symmetry) term $-a_a(A-2Z)^2/A$, a consequence of the Pauli principle and the charge symmetry of the nuclear force that penalises neutron–proton imbalance $N-Z=A-2Z$ (rooted in the symmetry of the nuclear Hamiltonian first analysed by Wigner [26]); and the *pairing* term δ, which captures the extra binding gained when like nucleons pair into spin-zero couples. We use the conventional $A^{-1/2}$ pairing form,

$$\delta(Z,N) \;=\; \begin{cases} +a_p\,A^{-1/2}, & Z \text{ even},\ N \text{ even} \quad \text{(even–even)}, \\ \;\;0, & A \text{ odd} \quad \text{(odd-}A\text{)}, \\ -a_p\,A^{-1/2}, & Z \text{ odd},\ N \text{ odd} \quad \text{(odd–odd)}. \end{cases} \tag{2}$$

Equation (1) is written with explicit minus signs so that all five fitted coefficients $\{a_v, a_s, a_c, a_a, a_p\}$ emerge positive. The binding energy per nucleon E_B/A follows by dividing by A.

2.3 Fitting procedure

A crucial feature of Eqs. (1)–(2) is that the total binding energy is *linear* in the five unknown coefficients. The problem can therefore be cast as a linear least-squares system $\mathbf{X}\,\boldsymbol{\beta} = \mathbf{y}$ with no need for iterative non-linear optimisation or starting guesses. For each nucleus i we form the row of the design matrix

$$\mathbf{X}_i = \Big[\,A_i,\ -A_i^{2/3},\ -\tfrac{Z_i(Z_i-1)}{A_i^{1/3}},\ -\tfrac{(A_i-2Z_i)^2}{A_i},\ s_i A_i^{-1/2}\,\Big], \qquad \boldsymbol{\beta} = \left(a_v, a_s, a_c, a_a, a_p\right)^{\top}, \tag{3}$$

where the pairing sign is $s_i = +1$ (even–even), 0 (odd-A), or -1 (odd–odd), and the target is $y_i = E_{B,i}^{\text{meas}} = A_i(E_B/A)_i$. The coefficients are obtained by *unweighted* ordinary least squares, minimising the residual sum of squares $\text{RSS} = \sum_i \left(y_i - \mathbf{X}_i\boldsymbol{\beta}\right)^2$, solved with the `numpy.linalg.lstsq` routine. The unweighted choice treats every nucleus equally and makes the fit a clean test of the *shape* of the mass surface rather than of the experimental error budget.

Parameter uncertainties were propagated from the ordinary-least-squares covariance matrix

$$\text{Cov}(\boldsymbol{\beta}) = \hat{\sigma}^2\,(\mathbf{X}^{\top}\mathbf{X})^{-1}, \qquad \hat{\sigma}^2 = \frac{\text{RSS}}{n-p}, \tag{4}$$

with n the number of nuclei and $p = 5$ parameters; the quoted standard errors are the square roots of the diagonal elements. Two fits were carried out: **Fit 1 (primary)** uses all 3487 nuclei with $A \geq 16$ (including AME extrapolations), and **Fit 2** is restricted to the 2484 experimentally measured nuclei. Fit 1 is adopted as the primary result because it provides the densest and most uniform sampling of the mass surface; Fit 2 serves as a sensitivity check on the influence of the extrapolated data.

Model quality is reported both on the total binding energy—through the root-mean-square error $\text{RMSE} = \sqrt{\text{RSS}/n}$ and the coefficient of determination R^2—and, as requested, through the RMS deviation of the predicted binding energy *per nucleon*,

$$\text{RMS}(E_B/A) = \sqrt{\frac{1}{n}\sum_{i=1}^{n}\left(\frac{E_{B,i}^{\text{meas}} - E_{B,i}^{\text{pred}}}{A_i}\right)^2}. \tag{5}$$

The per-nucleon residual $\Delta(E_B/A)_i = (E_{B,i}^{\text{meas}} - E_{B,i}^{\text{pred}})/A_i$ is the diagnostic used throughout the residual analysis of Section 4.

3 Results

3.1 Best-fit coefficients

Table 1 lists the five best-fit SEMF coefficients with their standard errors for both fits, together with representative literature values. The primary (Fit 1) coefficients are

$$a_v = (15.296 \pm 0.018)\,\text{MeV}, \quad a_s = (16.357 \pm 0.056)\,\text{MeV}, \quad a_c = (0.6917 \pm 0.0012)\,\text{MeV},$$
$$a_a = (22.30 \pm 0.04)\,\text{MeV}, \quad a_p = (11.39 \pm 0.87)\,\text{MeV}.$$

All five values sit comfortably within the ranges reported in standard references [21, 22, 27]: a volume term of $\sim$ 15–16 MeV, a surface term of $\sim$ 16–18 MeV, a Coulomb term near 0.7 MeV, an asymmetry term of $\sim$ 22–23 MeV, and a pairing term of order 11–12 MeV. The Coulomb coefficient is determined most sharply, to 0.17%, because the $Z(Z-1)/A^{1/3}$ term grows rapidly and is strongly constrained by the many heavy nuclei; the pairing coefficient is the least well-determined ($\sim$ 8% relative error), reflecting the small $A^{-1/2}$ amplitude of the odd–even staggering relative to the overall binding.

Table 1: Best-fit five-term SEMF coefficients (in MeV) from unweighted ordinary least-squares fits to AME2020 total binding energies ($A \geq 16$). Fit 1 uses all 3487 nuclei (including AME extrapolations); Fit 2 uses the 2484 experimentally measured nuclei. Uncertainties are 1σ standard errors from the least-squares covariance matrix.

Term	Symbol	Fit 1 (full, n=3487)	Fit 2 (exp. only, n=2484)	Literature
Volume	a_v	15.296 $\pm$ 0.018	15.414 $\pm$ 0.024	$\sim$ 15–16
Surface	a_s	16.357 $\pm$ 0.056	16.860 $\pm$ 0.074	$\sim$ 16–18
Coulomb	a_c	0.6917 $\pm$ 0.0012	0.6952 $\pm$ 0.0016	$\sim$ 0.70
Asymmetry	a_a	22.302 $\pm$ 0.042	22.497 $\pm$ 0.058	$\sim$ 22–23
Pairing	a_p	11.389 $\pm$ 0.866	12.028 $\pm$ 0.905	$\sim$ 11–12

Comparing the two fits provides a direct measure of the influence of the AME extrapolated masses. Excluding them (Fit 2) shifts the coefficients by at most about 0.5 MeV, the largest movements being in the surface (+0.50 MeV) and pairing (+0.64 MeV) terms, while the volume, Coulomb, and asymmetry terms change by 0.1–0.2 MeV or less. The extrapolated, mostly neutron-rich, drip-line nuclei thus exert only a modest pull on the macroscopic parameters, and the two fits are physically equivalent within the spread of published SEMF parameterisations.

3.2 Goodness of fit and the RMS deviation of E_B/A

The primary fit reproduces the total binding energies with an RMSE of 3.67 MeV and a coefficient of determination $R^2 = 0.99995$; because total binding energies range up to $\sim$ 1800 MeV, this corresponds to a relative accuracy of a few parts in a thousand, the well-known performance of the liquid-drop model. The quantity requested for this study, the RMS deviation of the predicted binding energy *per nucleon* evaluated over all fitted nuclei via Eq. (5), is

$$\boxed{\text{RMS}(E_B/A) = 0.0762\,\text{MeV/nucleon}} \qquad (\text{Fit 1, } n = 3487). \tag{6}$$

The experimental-only fit gives 0.0760 MeV/nucleon on its own 2484-nucleus subset, and 0.0803 MeV/nucleon when Fit 2 is applied to the full data set (a like-for-like comparison with Fit 1). The distribution of the per-nucleon residuals is narrow and nearly unbiased: mean −0.004 MeV/nucleon, median −0.003 MeV/nucleon, standard deviation 0.076 MeV/nucleon, with extremes of −0.34 and +1.14 MeV/nucleon. The largest positive outliers occur, significantly, at and near the magic numbers and in the light-mass region, as analysed in Section 4. This sub-0.1 MeV/nucleon scatter is not statistical noise but the coherent imprint of microscopic structure that the five-term model does not contain.

Figure 2a shows the binding energy per nucleon of all 3487 nuclei together with the SEMF prediction evaluated along the valley of β-stability, whose locus $Z^\star(A)$ follows the classic minimisation of the mass parabola [28].[1] The model captures the essential physics of the curve: the steep rise for light nuclei driven by the decreasing relative surface energy, the broad maximum of ≈ 8.8 MeV/nucleon in the iron region, and the slow decline toward heavy nuclei as the Coulomb term grows. The complementary decomposition in Fig. 2b shows how the constant volume term is progressively eroded by the surface term (dominant at low A), the Coulomb term (dominant at high A), and the asymmetry term (which grows along the neutron-rich stability line), leaving the smooth total that the fit reproduces.

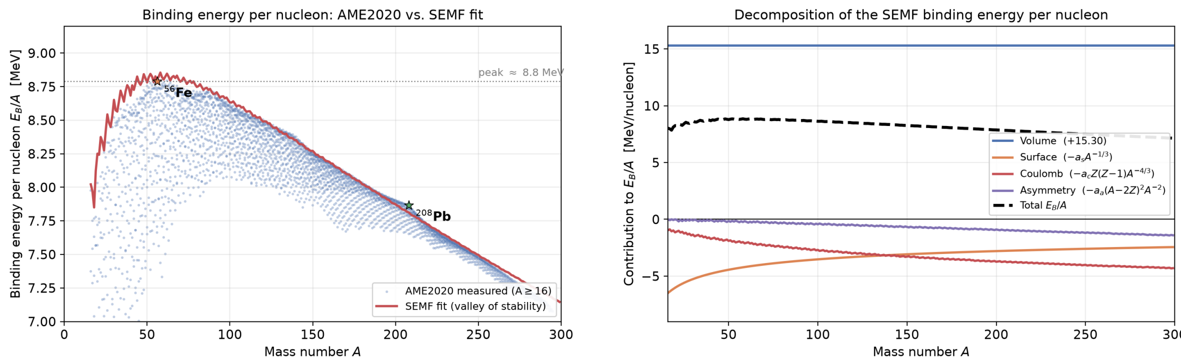

(a) Binding energy per nucleon E_B/A versus mass number A.

(b) Per-nucleon contribution of each SEMF term.

Figure 2: The liquid-drop binding-energy curve. (a) Measured E_B/A for all 3487 AME2020 nuclei with $A \geq 16$ (blue points) and the Fit 1 SEMF prediction evaluated along the valley of stability (red curve); the abundance peak ^{56}Fe and the doubly-magic ^{208}Pb are marked. (b) Decomposition of the fitted E_B/A into its volume, surface, Coulomb, and asymmetry contributions along the stability line, whose sum (black dashed) is the total binding energy per nucleon.

3.3 Case studies: ^{56}Fe and ^{208}Pb

Table 2 compares the measured and predicted binding energies for the two benchmark nuclei. ^{56}Fe ($Z = 26$, $N = 30$), which lies near the maximum of the binding-energy curve but at no magic number, is reproduced very well: the Fit 1 prediction of 494.80 MeV exceeds the measured 492.26 MeV by only 2.54 MeV (-0.52% on E_B, equivalently -0.045 MeV on E_B/A). The sign of this small discrepancy is a slight *over*binding by the smooth model, consistent with ^{56}Fe sitting just above the mid-shell region where no extra shell binding is available.

[1] For the plotted curves in Fig. 2 we use the standard β-stability approximation $Z^\star(A) = A/\big(1.98 + 0.0155\,A^{2/3}\big)$, rounded to the nearest integer; the fit itself uses the actual (Z, N) of every nucleus and does not depend on this relation.

Table 2: Measured versus SEMF-predicted binding energies for the case-study nuclei. Absolute error is $E_B^{\mathrm{pred}} - E_B^{\mathrm{meas}}$; a positive value means the model *under*predicts the binding. Predictions are given for both fits.

Nuclide	Z	N	A	E_B^{meas} (MeV)	E_B^{pred} (MeV)	ΔE_B (MeV)	rel. err. (%)
^{56}Fe	26	30	56	492.26	494.80	−2.54	−0.52
					493.44	−1.18	−0.24
^{208}Pb	82	126	208	1636.43	1625.23	11.20	0.68
					1626.23	10.20	0.62

First row of each nuclide: Fit 1 (full); second row: Fit 2 (experimental only).

The doubly-magic ^{208}Pb ($Z = 82$, $N = 126$) tells the opposite and more revealing story. The Fit 1 prediction of 1625.23 MeV falls short of the measured 1636.43 MeV by 11.20 MeV (+0.68%; +0.054 MeV on E_B/A): the model substantially *under*predicts the binding. This is not a failure of the fit but a physical signal. ^{208}Pb closes major shells in *both* the proton sector ($Z = 82$) and the neutron sector ($N = 126$) simultaneously, and the resulting doubly-magic configuration is extraordinarily tightly bound—by roughly 11 MeV more than any smooth function of A and Z can accommodate. The magnitude and sign of this residual are the single clearest demonstration in the data set that the liquid-drop model is missing shell structure, and they foreshadow the systematic pattern examined next.

4 Residual Analysis and Discussion

Figure 3 is the central diagnostic of this study: the per-nucleon residual $\Delta(E_B/A) = (E_B^{\mathrm{meas}} - E_B^{\mathrm{pred}})/A$ plotted against neutron number N for all 3487 nuclei, colour-coded by proton number Z, with the magic neutron numbers $N = 20, 28, 50, 82, 126$ marked. A well-specified macroscopic model would leave residuals scattered randomly about zero; instead the plot displays a highly organised structure. Across the medium- and heavy-mass region the residuals trace smooth arcs that swing positive as each magic number is approached and dip negative in the mid-shell regions between them, producing distinct positive *ridges* centred on $N = 28, 50, 82$ and 126. In the light region ($N \lesssim 28$) the scatter is much larger and predominantly positive, reaching up to +1.1 MeV/nucleon, reflecting the well-known deterioration of the liquid-drop approximation for the lightest nuclei, where surface and curvature corrections beyond the $A^{2/3}$ term become important [29] and individual light nuclei are poorly described by a bulk-matter picture.

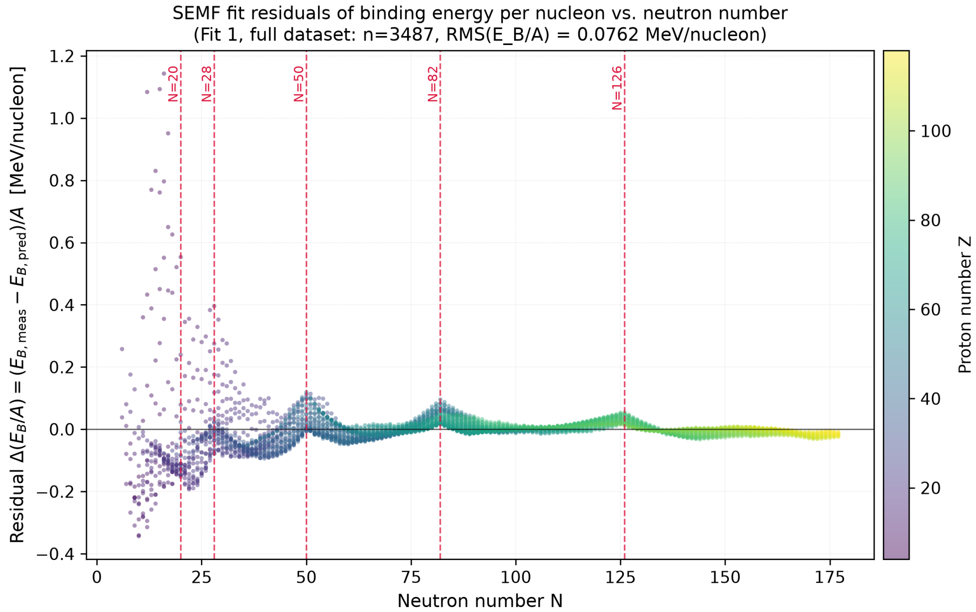

Figure 3: SEMF fit residuals versus neutron number. Per-nucleon residual $\Delta(E_B/A) = (E_{B,\text{meas}} - E_{B,\text{pred}})/A$ for all 3487 AME2020 nuclei with $A \geq 16$ (Fit 1), colour-coded by proton number Z. Red dashed lines mark the magic neutron numbers $N = 20, 28, 50, 82, 126$. Systematic positive residual peaks appear at $N = 28, 50, 82, 126$: at these shell closures the model *underpredicts* the binding energy, the characteristic fingerprint of nuclear shell structure superimposed on the smooth liquid-drop baseline. The large positive scatter at low N marks the light-nucleus region where the macroscopic approximation is weakest.

To quantify the effect, Table 3 compares, for each magic neutron number, the mean residual of the nuclei lying exactly at that N with the mean residual of a local background of nuclei within ± 4 neutrons. At $N = 28, 50, 82$, and 126 the mean residual is positive and exceeds its local background by $+0.008$ to $+0.034\,\text{MeV}/nucleon$; the enhancement is largest at $N = 28$ and decreases toward the heaviest shell, as expected since the same $\sim$MeV shell-gap energy is spread over a larger nucleon number A and so produces a smaller per-nucleon signal. The neutron shell at $N = 20$ is the sole exception: its at-magic mean residual is slightly *below* the local background, because $N = 20$ nuclei fall in the light, high-scatter region where the large, structurally distinct light-nucleus residuals dominate over the comparatively modest *sd*-shell gap. The four heavier closures ($N = 28, 50, 82, 126$) therefore constitute the clean, unambiguous locations where the model *most systematically fails*.

Table 3: Residual enhancement at the magic neutron numbers (Fit 1). "At N" is the mean per-nucleon residual of nuclei with exactly that neutron number; "background" is the mean over nuclei within ± 4 neutrons; the enhancement is their difference. A positive enhancement signals extra binding (model underprediction) at the shell closure.

Magic N	# nuclei at N	Mean at N (MeV/nuc.)	Background (± 4) (MeV/nuc.)	Enhancement (MeV/nuc.)	Status
20	21	−0.0441	−0.0315	−0.0127	light-region scatter
28	23	0.0266	−0.0078	0.0344	clear positive peak
50	25	0.0385	0.0159	0.0226	clear positive peak
82	29	0.0416	0.0267	0.0149	clear positive peak
126	18	0.0303	0.0219	0.0084	clear positive peak

The same signal is displayed in the plane of the nuclear chart in Fig. 4, which maps the residual as a function of both N and Z. Vertical red (underbound) ridges run along the neutron magic numbers, and the deepest red concentrations sit at the intersections with the proton magic numbers—most strikingly at $(N, Z) = (126, 82)$, i.e. ^{208}Pb, and along $N = 82$ near $Z = 50$ (the doubly-magic ^{132}Sn region). This two-dimensional view confirms that the residual structure is governed by shell closures in both nucleon species rather than by any deficiency tied to mass number alone.

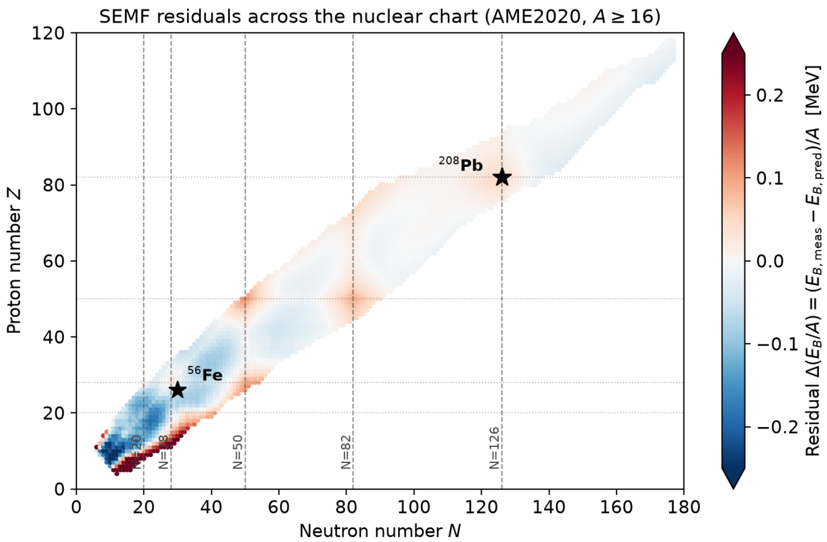

Figure 4: Residuals across the nuclear chart. SEMF per-nucleon residual mapped in the (N, Z) plane (Fit 1). Red indicates model underprediction (extra binding), blue overprediction. Dashed lines mark magic neutron numbers and dotted lines magic proton numbers; ^{56}Fe and ^{208}Pb are starred. Underbound (red) ridges align with the magic numbers, and the strongest signal occurs at doubly-magic intersections such as ^{208}Pb (N=126, Z=82).

Physical interpretation. The systematic failure of the model at $N = 28, 50, 82, 126$ is the direct manifestation of **nuclear shell structure**. In the shell model, nucleons occupy discrete single-particle orbitals grouped into shells separated by large energy gaps; the strong spin–orbit interaction identified by Goeppert Mayer [6] and Haxel, Jensen, and Suess [7] reorders these orbitals so that the gaps fall precisely at the magic numbers $2, 8, 20, 28, 50, 82, 126$. When a neutron (or proton) number equals a magic value, the corresponding shell is filled, the next nucleon must be placed across a wide energy gap, and the nucleus is anomalously stable and tightly bound. The liquid-drop model of Eq. (1), being a smooth function of the bulk variables A and Z with no reference to single-particle orbitals, has no mechanism to generate this extra binding. It therefore *underpredicts* E_B at the shell closures, producing the positive residual peaks observed in Figs. 3 and 4 and the $+11.2$ MeV deficit for ^{208}Pb. Conversely, in the open mid-shell regions the collective deformation and configuration mixing not captured by the spherical drop lead to slight overbinding, giving the negative excursions between the ridges.

This is exactly the discrepancy—customarily termed the *shell correction*—that the Strutinsky energy theorem isolates and adds back to a macroscopic energy in the macroscopic–microscopic method [9, 10]. Modern global mass models that incorporate such corrections, including the finite-range droplet model [11, 12], the Weizsäcker–Skyrme models [13], the Duflo–Zuker formula [14], and Hartree–Fock–Bogoliubov mass tables [15], reduce the RMS mass deviation from the several-MeV level of the bare liquid-drop model to a few hundred keV, precisely by supplying the shell (and deformation and pairing-fluctuation) physics whose absence is diagnosed here [1, 30]. The residual structure we obtain is thus not merely an error budget but a physically meaningful map of where microscopic effects matter most, information now also exploited as prior physics in machine-learning mass models [23, 24] and essential for the mass inputs of r-process nucleosynthesis [16, 17].

5 Conclusions

We have fitted the five-term semi-empirical (liquid-drop) mass formula to the total binding energies of all 3487 nuclei with $A \geq 16$ in the **AME2020** atomic mass evaluation (release dated 3 March 2021; *Chinese Physics C* **45**, 030002/030003), obtained from the IAEA Atomic Mass Data Center. The unweighted least-squares fit yields $a_v = (15.296 \pm 0.018)$ MeV, $a_s = (16.357 \pm 0.056)$ MeV, $a_c = (0.6917 \pm 0.0012)$ MeV, $a_a = (22.30 \pm 0.04)$ MeV, and $a_p = (11.39 \pm 0.87)$ MeV, all in accord with accepted values. The model reproduces the total binding energies with $R^2 = 0.99995$ and an RMS deviation of the binding energy per nucleon of 0.0762 MeV/nucleon across all fitted nuclei. The abundance-peak nucleus ^{56}Fe is reproduced to 0.52% (predicted 494.80 MeV vs. measured 492.26 MeV), while the doubly-magic ^{208}Pb is underpredicted by 11.20 MeV (0.68%; predicted 1625.23 MeV vs. measured 1636.43 MeV).

The residual analysis is the physically decisive result. Plotted against neutron number, the per-nucleon residuals are not random but display systematic positive peaks at the magic neutron numbers $N = 28, 50, 82, 126$, where the model most systematically fails, with the effect seen equally clearly at the proton magic numbers in the two-dimensional chart. The responsible physical mechanism is **nuclear shell structure**: the closure of a major shell confers extra binding that the smooth macroscopic liquid-drop model omits by construction. The principal limitations of the SEMF follow directly—it cannot describe shell closures, magic numbers, ground-state deformation, or the finer details of the light-mass region—and its few-MeV residual is exactly the shell-correction energy supplied by the microscopic shell model and by modern macroscopic–microscopic and self-consistent mass models. The liquid-drop model thus remains an outstanding baseline whose very failures, made quantitative here, point precisely to the quantum physics of nucleonic shells.

Data and code availability

The analysis is fully reproducible. The AME2020 mass table (`mass_1.mas20.txt`) was obtained from the IAEA Atomic Mass Data Center. Parsing, fitting, and evaluation scripts (`01_parse_ame2020.py`, `02_fit_semf.py`, `03_analyze_residuals.py`) and the machine-readable outputs (`ame2020_cleaned.csv`, `semf_fit_results.json`, `model_evaluation.json`) accompany this report.

References

[1] David Lunney, J. M. Pearson, and C. Thibault. Recent trends in the determination of nuclear masses. *Reviews of Modern Physics*, 75(3):1021–1082, 2003. doi: 10.1103/RevModPhys.75.1021.

[2] G. Gamow. Mass defect curve and nuclear constitution. *Proceedings of the Royal Society of London. Series A*, 126(803):632–644, 1930. doi: 10.1098/rspa.1930.0032.

[3] C. F. von Weizsäcker. Zur theorie der kernmassen. *Zeitschrift für Physik*, 96(7–8):431–458, 1935. doi: 10.1007/BF01337700.

[4] H. A. Bethe and R. F. Bacher. Nuclear physics A. stationary states of nuclei. *Reviews of Modern Physics*, 8(2):82–229, 1936. doi: 10.1103/RevModPhys.8.82.

[5] N. Bohr and J. A. Wheeler. The mechanism of nuclear fission. *Physical Review*, 56(5):426–450, 1939. doi: 10.1103/PhysRev.56.426.

[6] Maria Goeppert Mayer. On closed shells in nuclei. II. *Physical Review*, 75(12):1969–1970, 1949. doi: 10.1103/PhysRev.75.1969.

[7] Otto Haxel, J. Hans D. Jensen, and Hans E. Suess. On the “magic numbers” in nuclear structure. *Physical Review*, 75(11):1766, 1949. doi: 10.1103/PhysRev.75.1766.2.

[8] Aage Bohr and Ben R. Mottelson. *Nuclear Structure, Volume I: Single-Particle Motion*. W. A. Benjamin, New York, 1969. ISBN 978-0-8053-1016-0.

[9] V. M. Strutinsky. Shell effects in nuclear masses and deformation energies. *Nuclear Physics A*, 95(2):420–442, 1967. doi: 10.1016/0375-9474(67)90510-6.

[10] W. D. Myers and W. J. Swiatecki. Nuclear masses and deformations. *Nuclear Physics*, 81 (1):1–60, 1966. doi: 10.1016/S0029-5582(66)80001-9.

[11] P. Möller, J. R. Nix, W. D. Myers, and W. J. Swiatecki. Nuclear ground-state masses and deformations. *Atomic Data and Nuclear Data Tables*, 59(2):185–381, 1995. doi: 10.1006/adnd.1995.1002.

[12] P. Möller, A. J. Sierk, T. Ichikawa, and H. Sagawa. Nuclear ground-state masses and deformations: FRDM(2012). *Atomic Data and Nuclear Data Tables*, 109–110:1–204, 2016. doi: 10.1016/j.adt.2015.10.002.

[13] Ning Wang, Min Liu, Xizhen Wu, and Jie Meng. Surface diffuseness correction in global mass formula. *Physics Letters B*, 734:215–219, 2014. doi: 10.1016/j.physletb.2014.05.049.

[14] J. Duflo and A. P. Zuker. Microscopic mass formulae. *Physical Review C*, 52(1):R23–R27, 1995. doi: 10.1103/PhysRevC.52.R23.

[15] S. Goriely, N. Chamel, and J. M. Pearson. Skyrme-hartree-fock-bogoliubov nuclear mass formulas: Crossing the 0.6 MeV accuracy threshold with microscopically deduced pairing. *Physical Review Letters*, 102(15):152503, 2009. doi: 10.1103/PhysRevLett.102.152503.

[16] M. R. Mumpower, R. Surman, G. C. McLaughlin, and A. Aprahamian. The impact of individual nuclear properties on r-process nucleosynthesis. *Progress in Particle and Nuclear Physics*, 86:86–126, 2016. doi: 10.1016/j.ppnp.2015.09.001.

[17] John J. Cowan, Christopher Sneden, James E. Lawler, Ani Aprahamian, Michael Wiescher, Karlheinz Langanke, Gabriel Martínez-Pinedo, and Friedrich-Karl Thielemann. Origin of the heaviest elements: The rapid neutron-capture process. *Reviews of Modern Physics*, 93 (1):015002, 2021. doi: 10.1103/RevModPhys.93.015002.

[18] W. J. Huang, Meng Wang, F. G. Kondev, G. Audi, and S. Naimi. The AME 2020 atomic mass evaluation (I). evaluation of input data, and adjustment procedures. *Chinese Physics C*, 45(3):030002, 2021. doi: 10.1088/1674-1137/abddb0.

[19] Meng Wang, W. J. Huang, F. G. Kondev, G. Audi, and S. Naimi. The AME 2020 atomic mass evaluation (II). tables, graphs and references. *Chinese Physics C*, 45(3):030003, 2021. doi: 10.1088/1674-1137/abddaf.

[20] F. G. Kondev, M. Wang, W. J. Huang, S. Naimi, and G. Audi. The NUBASE2020 evaluation of nuclear physics properties. *Chinese Physics C*, 45(3):030001, 2021. doi: 10.1088/1674-1137/abddae.

[21] Michael W. Kirson. Mutual influence of terms in a semi-empirical mass formula. *Nuclear Physics A*, 798(1–2):29–60, 2008. doi: 10.1016/j.nuclphysa.2007.10.011.

[22] D. Benzaid, S. Bentridi, A. Kerraci, and N. Amrani. Bethe-weizsäcker semiempirical mass formula coefficients 2019 update based on AME2016. *Nuclear Science and Techniques*, 31 (1):9, 2020. doi: 10.1007/s41365-019-0718-8.

[23] R. Utama, J. Piekarewicz, and H. B. Prosper. Nuclear mass predictions for the crustal composition of neutron stars: A bayesian neural network approach. *Physical Review C*, 93 (1):014311, 2016. doi: 10.1103/PhysRevC.93.014311.

[24] A. E. Lovell, A. T. Mohan, T. M. Sprouse, and M. R. Mumpower. Nuclear masses learned from a probabilistic neural network. *Physical Review C*, 106(1):014305, 2022. doi: 10.1103/PhysRevC.106.014305.

[25] G. Audi, F. G. Kondev, Meng Wang, W. J. Huang, and S. Naimi. The NUBASE2016 evaluation of nuclear properties. *Chinese Physics C*, 41(3):030001, 2017. doi: 10.1088/1674-1137/41/3/030001.

[26] E. Wigner. On the consequences of the symmetry of the nuclear hamiltonian on the spectroscopy of nuclei. *Physical Review*, 51(2):106–119, 1937. doi: 10.1103/PhysRev.51.106.

[27] Kenneth S. Krane. *Introductory Nuclear Physics*. John Wiley & Sons, New York, 1988. ISBN 978-0-471-80553-3.

[28] Alex E. S. Green. Coordinates of the most stable nuclei. *Physical Review*, 95(1):161–164, 1954. doi: 10.1103/PhysRev.95.161.

[29] K. Pomorski and J. Dudek. Nuclear liquid-drop model and surface-curvature effects. *Physical Review C*, 67(4):044316, 2003. doi: 10.1103/PhysRevC.67.044316.

[30] A. Sobiczewski, Yu. A. Litvinov, and M. Palczewski. Detailed comparison of theoretical nuclear-mass tables. *Atomic Data and Nuclear Data Tables*, 119:1–49, 2018. doi: 10.1016/j.adt.2017.10.001.